Draft version March 3, 2014
Preprint typeset using LaTeX style emulateapj v. 04/17/13

arXiv:1402.7264v1 [astro-ph.GA] 27 Feb 2014

THE PANCHROMATIC HUBBLE ANDROMEDA TREASURY V: AGES AND MASSES OF THE YEAR 1 STELLAR CLUSTERS

Morgan Fouesneau[1], L. Clifton Johnson[1], Daniel R. Weisz[1,2,13], Julianne J. Dalcanton[1], Eric F. Bell[3], Luciana Bianchi[4] Nelson Caldwell[5], Dimitrios A. Gouliermis[6,7] Puragra Guhathakurta[8], Jason Kalirai[9], Søren S. Larsen[10], Hans-Walter Rix[7], Anil C. Seth[11], Evan D. Skillman[12], and Benjamin F. Williams[1]

Draft version March 3, 2014

ABSTRACT

We present ages and masses for 601 star clusters in M31 from the analysis of the six filter integrated light measurements from near ultraviolet to near infrared wavelengths, made as part of the Panchromatic Hubble Andromeda Treasury (PHAT). We derive the ages and masses using a probabilistic technique, which accounts for the effects of stochastic sampling of the stellar initial mass function. Tests on synthetic data show that this method, in conjunction with the exquisite sensitivity of the PHAT observations and their broad wavelength baseline, provides robust age and mass recovery for clusters ranging from $\sim 10^2 - 2\times10^6$ M$_\odot$. We find that the cluster age distribution is consistent with being uniform over the past 100 Myr, which suggests a weak effect of cluster disruption within M31. The age distribution of older (> 100 Myr) clusters fall towards old ages, consistent with a power-law decline of index -1, likely from a combination of fading and disruption of the clusters. We find that the mass distribution of the whole sample can be well-described by a single power-law with a spectral index of -1.9 ± 0.1 over the range of $10^3 - 3\times10^5$ M$_\odot$. However, if we subdivide the sample by galactocentric radius, we find that the age distributions remain unchanged. However, the mass spectral index varies significantly, showing best fit values between -2.2 and -1.8, with the shallower slope in the highest star formation intensity regions. We explore the robustness of our study to potential systematics and conclude that the cluster mass function may vary with respect to environment.

Subject headings: Galaxies: Individual (M31), Star clusters — Methods: data analysis, statistical — Techniques: photometric

1. INTRODUCTION

It has become clear that a significant fraction of star formation occurs in stellar clusters. However, deriving galaxy histories from observations of clusters is complicated by significant uncertainties. Controversial questions have been raised regarding cluster properties in various environments as different analyses could lead to different conclusions. Claims exists for interesting variations or trends in cluster colors, their lifetimes as gravitationally bound objects, and age or mass distributions within or between galaxies, and the evolution from initial to current cluster mass functions (e.g., Zepf & Ashman 1993; Kumai et al. 1993; Girardi et al. 1995; Elmegreen & Efremov 1997; Bastian et al. 2011).

Such studies rely on our ability to estimate intrinsic properties of stellar clusters, in particular, their ages and masses. Much observational effort has therefore been invested in determining the distributions of star cluster ages and masses (Searle et al. 1980; Larsen & Richtler 2000; Billett et al. 2002; Hunter et al. 2003; Fall et al. 2005; Rafelski & Zaritsky 2005; Dowell et al. 2008; Larsen 2009; Chandar et al. 2010; Bastian et al. 2012), and using the resulting data to determine the dominant mechanisms of cluster formation and disruption (Kroupa & Boily 2002; Boutloukos & Lamers 2003; Lamers et al. 2005; Whitmore et al. 2007; Parmentier & de Grijs 2008; Fall et al. 2009; Elmegreen & Hunter 2010; Converse & Stahler 2011). However, most of the existing work deals with observations of relatively massive clusters (a few $10^4 - 10^5$ M$_\odot$), which are the least affected by disruption processes and thus are the most stable in various environments. As a result, divergences between disruption models (e.g. Baumgardt & Makino 2003; Fall et al. 2009, among many others) are still subject to debate in the literature (e.g. Whitmore et al. 2011; Silva-Villa et al. 2014, most recently in M83). Only a few studies have been able to probe the smaller clusters that are the most sensitive to environmental effects (mainly in the Galaxy, e.g., Borissova et al. 2011, or the Magellanic Clouds, e.g.,

mfouesn@astro.washingtonedu
[1] Department of Astronomy, University of Washington, Seattle, Washington, USA
[2] Department of Astronomy, University of California at Santa Cruz, 1156 High Street, Santa Cruz, CA, 95064
[3] Department of Astronomy, University of Michigan, 500 Church Street, Ann Arbor, MI 48109, USA
[4] Department of Physics and Astronomy, Johns Hopkins University, Baltimore, MD 21218, USA
[5] Harvard-Smithsonian Center for Astrophysics, 60 Garden Street Cambridge, MA 02138, USA
[6] Institut für Theoretische Astrophysik, Zentrum für Astronomie der Universität Heidelberg, Albert-Ueberle-Strasse 2, 69120 Heidelberg, Germany
[7] Max-Planck-Institut für Astronomie, Königstuhl 17, 69117 Heidelberg, Germany
[8] University of California Observatories/Lick Observatory, University of California, 1156 High Street, Santa Cruz, CA 95064, USA
[9] Space Telescope Science Institute, 3700 San Martin Drive, Baltimore, MD 21218, USA
[10] Department of Astrophysics, IMAPP, Radboud University Nijmegen, P.O. Box 9010, 6500 GL Nijmegen, The Netherlands
[11] Department of Physics and Astronomy, University of Utah, Salt Lake City, UT 84112, USA
[12] Department of Astronomy, University of Minnesota, 116 Church Street SE, Minneapolis, MN 55455, USA
[13] Hubble Fellow

Popescu et al. 2012).

The Panchromatic Hubble Andromeda Treasury (PHAT; Dalcanton et al. 2012) is an ongoing multi-cycle Hubble Space Telescope (HST) program that is ideal for studying stellar clusters in M31. The survey imaged one-third of the M31 disk at high spatial resolution with wavelength coverage from the ultraviolet through the near-infrared. The sensitivity of the latest HST instruments allow us to detect clusters in M31 down to a regime in which cluster luminosities overlap those of individual bright stars, and hence to very low masses (Johnson et al. 2012). This survey spans a wide range of environments in both star formation intensities and gas densities. This diversity is an advantage for addressing how environment affects cluster formation.

The PHAT survey has already significantly increased the number of clusters known in M31. Johnson et al. (2012) identified 601 stellar clusters using the first quarter of the total PHAT coverage. This new cluster catalog contains more than a factor of four increase in the number of known clusters within the survey area. Moreover, the uniform photometric coverage from the UV to near-IR allows accurate age-dating of the clusters. Even this preliminary sample breaks new ground for studying clusters outside the Milky Way and the Magellanic Clouds, probing about two orders of magnitudes fainter in the luminosity function (Johnson et al. 2012, their figure 11).

This paper is part of a series utilizing the PHAT dataset for studies of stellar clusters. Johnson et al. (2012) presented the first installment of a HST-based cluster catalog, which serves as the basis for an extensive study of Andromeda's cluster population. In this paper, we focus on the determination of ages and masses of the first year sample, looking forward to the final product of this four year Treasury program. Our estimates of the properties of the clusters are derived from integrated photometry in six broad bands and we especially focus our attention on the characterization of the lowest-mass clusters. Additional studies, including analysis of structural parameters, resolved star content, and integrated spectroscopy of the cluster sample will follow in subsequent work.

This paper is organized as follows. §2 presents the cluster sample and the key elements of their photometry. §3 describes the analysis and the cluster models used to derive the properties of the clusters, and briefly highlights the possible artifacts of the method using synthetic data. §4 describes our results for the entire sample and for individual regions across M31. Finally, we discuss those results in §5 before drawing our conclusions.

2. OBSERVATIONS & CLUSTER CATALOG

For this paper, we use the list of 601 high-probability cluster candidates from the Johnson et al. (2012) Year 1 catalog, which contains integrated photometry through six broad-band filters from the UV to the near infrared: F275W (UV), F336W (U), F475W (g), F814W (I), F110W (J), F160W (H). Clusters were detected by-eye, primarily based on the F475W images, and visually classified based on their sizes, shapes, and concentrations as explained in Johnson et al. (2012).

The Year 1 catalog is sub-divided into regions called "bricks", following the survey observation strategy described in Dalcanton et al. (2012). The cluster catalog includes four full bricks (designated B01, B09, B15, and B21; numbers increase with increasing galactocentric radius) as well as the western halves of two additional bricks (B17W and B23W). For simplicity, we group B17W with B15 and B23W with B21, respectively, for the remainder of this work, since both pairs form contiguous regions. These data sample locations along the major axis of M31, covering the bulge (B01) and regions at at ~ 6, 10, and 15 kpc from the center of the galaxy (B09, B15, and B21, respectively). With the exception of the bulge-dominated brick, B01, the remaining ones target regions of high star formation, located on the star forming ring (B15) or on spiral arms (B09, B21). Of the three disk fields, B15 samples the highest star formation intensity, found in the "10 kpc-ring". The color image in Fig. 1 illustrates the positions of the clusters in the catalog in the different observed regions, relative to the expected final coverage of the survey.

Measurement details are described in § 4 of Johnson et al. (2012), we briefly summarize the different steps in the following. We measured instrumental magnitudes for the clusters using aperture photometry. Measurements were converted into the VEGA magnitude system (see Johnson et al. 2012, §4.1.1 for details). We do not perform passband conversions and instead work with the native HST filters. For each object, circular aperture photometry produced integrated flux values, and aperture radii vary from cluster to cluster between $0.5''$ (1.9 pc) and $6''$ (22.7 pc). Measurement uncertainties are typically lower than 0.2 mag, for which we include background measurement uncertainties. Aperture corrections were based on their half-light radius in the F475W images, assuming flat radial color profiles in the outer parts of the clusters. Typical correction values are ~ 0.1 mag. We assume a distance to M31 of 785 kpc (McConnachie et al. 2005), which corresponds to a distance modulus of $m - M = 24.47$ mag.

Assessing the completeness of cluster samples is a challenge on its own. The true completeness of the sample as a whole is a complicated function of cluster luminosity, size, and location within M31. The completeness of the sample was assessed by conducting artificial cluster tests. Briefly, we used synthetic clusters that span the range of properties expected for the cluster sample. Specifically, we sampled ages from 4 million to 10 billion years and masses from 10^2 to 10^5 $M_\odot$, and cluster half-light radii (assuming King 1962 profiles) of $1-7$ pc (§3.1 of Johnson et al. 2012, especially their Fig. 6). On average, the 50% completeness limits in the F475W filter are $M_{F475W} = -3.8$, -3.5, -2.8, -2.2 for B01, B09, B15, and B21, respectively.

3. DERIVING CLUSTER PROPERTIES

In this section, we derive cluster ages and masses using the probabilistic method developed in Fouesneau & Lançon (2010). The method is based on a large collection of Monte-Carlo simulations of individual clusters. These simulations take full account of stochastic sampling of the stellar mass distribution, allowing robust Bayesian fitting to the observed colors of the observed clusters, even for the low mass regime.

3.1. *Population models*

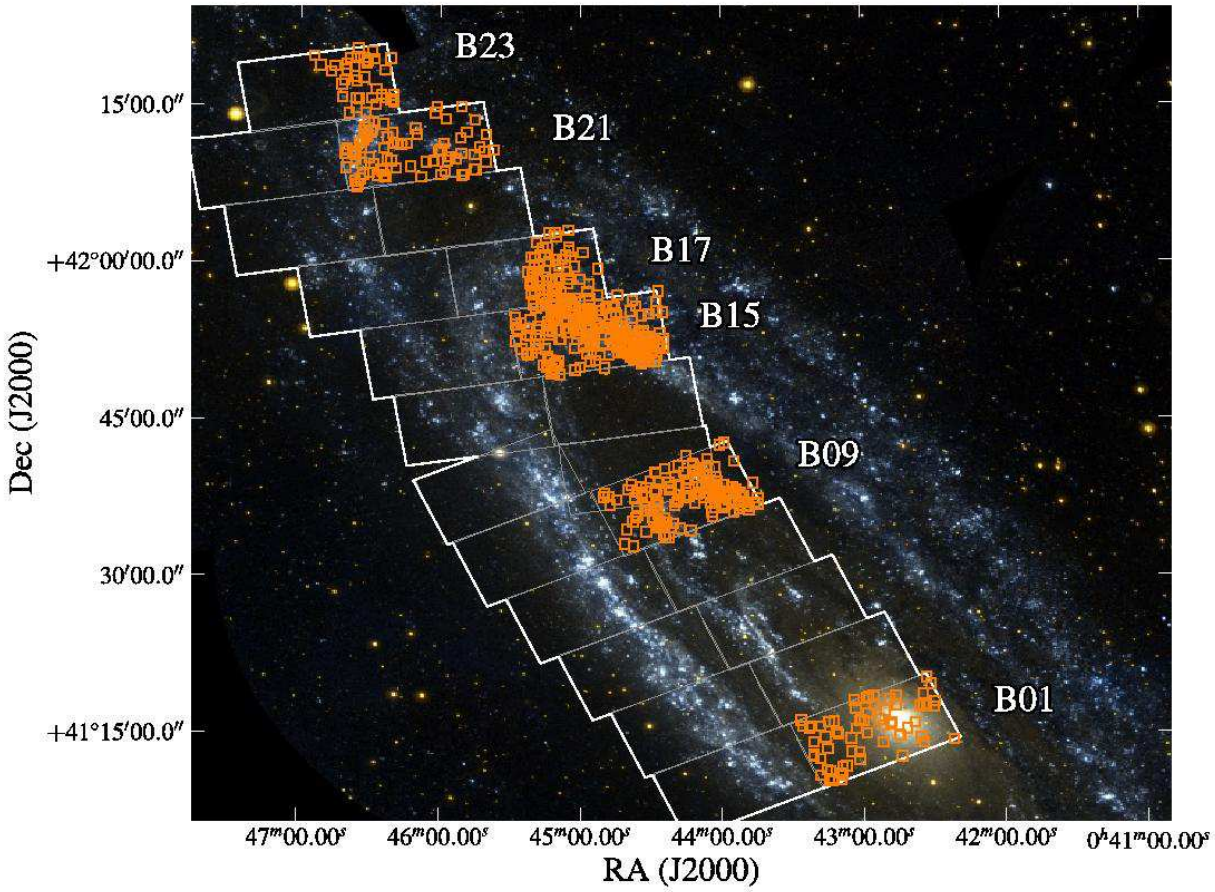

FIG. 1.— GALEX FUV/NUV composite image showing the positions of the clusters (orange squares) in the PHAT Year 1 Catalog. The white outer contour illustrates the footprint of the final survey, subdivided into rectangular "bricks" (1.5×2.7 kpc), shown in grey. Labels correspond to the names of the regions mentioned in § 2.

Synthetic spectral energy distributions (SEDs) of clusters are constructed with the population synthesis code `Pégase.2n` (Fouesneau et al. in prep.), which is derived from `Pégase` (Fioc & Rocca-Volmerange 1997). As in the original population synthesis code, the underlying stellar evolution tracks are those of the Padova group (Bressan et al. 1993; Bertelli et al. 1994), with a simple extension through the thermally pulsating AGB based on the prescriptions of Groenewegen & de Jong (1993). The input stellar spectra are taken from the library of Lejeune et al. (1997). The stellar initial mass function (IMF) is taken from Kroupa et al. (1993), and extends from 0.1 to 120 $M_\odot$. Nebular emission (lines and continuum) are computed as in Fioc & Rocca-Volmerange (1997) and are included in the calculated spectra and broad band fluxes under the assumption that no ionizing photons escape. The photometry for the synthetic clusters is computed using the response curves of the PHAT HST/ACS and HST/WFC3 filters. A reference spectrum of Vega provides zero magnitude fluxes (Bohlin 2007).

The code uses Monte-Carlo (MC) methods to populate the stellar mass function (SMF) with a finite number of stars. The simulations draw an explicit number of stars instead of a target mass which avoids the possible biases linked to the latter case (Kroupa et al. 2013). As a result, models explicitly account for stochastic variations in the stellar content of clusters. We have extended the simulated cluster set to lower masses than available in Fouesneau et al. (2012), and the coverage now ranges from ~ 50 to 5×10^5 $M_\odot$, and ages from 1 Myr to 20 Gyr. With a few $\times 10^8$ individual models, the collection of synthetic clusters is large enough to include all reasonably likely cluster properties.

We also include a transition to continuous models above 2×10^5 $M_\odot$ (*i.e.*, models assuming a continuously populated stellar mass function), motivated by the presence of about ~ 30 massive globular clusters in the PHAT catalog ($> 10^5$ $M_\odot$, Caldwell et al. 2011). For computational reasons discussed in Fouesneau et al. (2012), the mass distribution in the collection of models follows a power law of index -1. The ages of the synthetic clusters are drawn from a power law distribution with index -1 (equal numbers per logarithmic bin), rounded to integer multiples of 10^6 yr. The extinction, A_V, is allowed to vary uniformly from 0 to 3 magnitudes with a fixed R_V of 3.1 assuming the standard extinction law of Cardelli et al. (1989).

Based on HII region abundances (e.g., Zurita & Bresolin 2012), we expect young clusters in M31 to have approximatively solar metallicity. Thus, we fix the metallicity, Z, to 0.02 (solar) for the discrete part of the collection. In contrast, globular clusters are known to have lower metallicities (e.g., Caldwell et al. 2011; Cezario et al. 2012), and thus the metallicity

of the continuous models for massive clusters is allowed to vary (equiprobably) between the fixed values of $[0.004, 0.008, 0.02, 0.05]$, corresponding approximately to Small and Large Magellanic Clouds, Solar, and super-Solar metallicities, respectively.

Individual cluster estimates are collected into Table 2 in Appendix A.

3.2. *Analysis Method*

The probabilistic method developed in Fouesneau & Lançon (2010) calculates posterior probability distributions in the age-mass-extinction space (marginalized over the metallicity dimension), using multi-wavelength photometric observations and the large collection of Monte-Carlo simulations of clusters of finite stellar masses, described above. As in all Bayesian inference approaches, the results are stated in probabilistic terms, and they depend on *a priori* probability distributions of some model parameters (priors).

In our context, the probability for one cluster to have a specific age, mass, extinction, and metallicity, given a set of photometric observations is:

$$\mathcal{P}(\overrightarrow{\theta} \mid \overrightarrow{d}, \overrightarrow{\sigma}) \propto \mathcal{P}(\overrightarrow{d} \mid \overrightarrow{\theta}, \overrightarrow{\sigma}) \times \mathcal{P}(\overrightarrow{\theta}), \quad (1)$$

where the $\overrightarrow{d}$ and $\overrightarrow{\sigma}$ are the 6 band photometric measurements and associated uncertainties, $\overrightarrow{\theta}$ is the ensemble of parameter values (*i.e.*, age-mass-extinction-metallicity), $\mathcal{P}(\overrightarrow{\theta})$ are the priors on the values of the parameters $\overrightarrow{\theta}$, and $\mathcal{P}(\overrightarrow{d} \mid \overrightarrow{\theta}, \overrightarrow{\sigma})$ is the likelihood of measuring an energy distribution for a given set of $\overrightarrow{\theta}$.

Likelihood— We adopt a normal based-likelihood function, assuming the photometric errors are Gaussian and independent flux measurements:

$$\mathcal{P}(\overrightarrow{d} \mid \overrightarrow{\theta}) = \prod_{k=1}^{6} \frac{1}{\sqrt{2\pi}\sigma_k} \exp\left[-\frac{\left(d_k - \hat{d}_k(\overrightarrow{\theta})\right)^2}{2\,\sigma_k^2} \right] \quad (2)$$

in which k indicates properties for the k-th filter, and $\hat{d}_k(\overrightarrow{\theta})$ the predicted flux in the filter k for the given set of $\overrightarrow{\theta}$.

Priors— The posterior probability distribution, $\mathcal{P}(\overrightarrow{\theta} \mid \overrightarrow{d})$, depends on the prior constraints on the values of the parameters $\overrightarrow{\theta}$. This prior information translates the age and mass distributions of the synthetic clusters, together with the values allowed for extinction. As described in § 3.1, our priors can be explicitly expressed as an independent combination of age, mass, and extinction functions:

$$\mathcal{P}(\overrightarrow{\theta}) \propto (M/\ \mathrm{M}_\odot)^{-1} \times (A/\ \mathrm{yr})^{-1}, \quad (3)$$

corresponding to independent power-laws in age and mass, and implicitly uniform in A_V, respectively. The completeness limits of the observations are not used in any manner during the determination of individual ages and masses. The power-law distributions we have adopted mimic two major qualitative trends seen in star-forming galaxies: low mass clusters are more numerous than high mass clusters, and, because of a variety of efficient disruption mechanisms, young clusters are more numerous than old ones. As demonstrated in Fouesneau et al. (2012), the priors do not globally dominate the resulting behavior of $\mathcal{P}(\overrightarrow{\theta} \mid \overrightarrow{d}, \overrightarrow{\sigma})$ (Eqn. 1). A study based on the full survey will further optimize the prior distributions, in particular age-mass, to derive cluster disruption efficiencies across the covered area of M31.

An illustrative example of the method for a typical cluster is given Fig. 2. A composite image of the cluster is shown in panel (a). We show the cluster color magnitude diagram (CMD) in panel (b), on which the gray density map in the background represent the possible contamination by the field stars. On this CMD, we overlaid a blue isochrone corresponding to the best fit value from the integrated photometry analysis accounting for age-mass-extinction correlations. We represent the correlation between age and mass by the joined age-mass probability distribution function (PDF) in panel (c) of Fig. 2, marginalized over the extinction parameter, A_V.

In panel (d) of Figure 2, we demonstrate the possible effect of A_V by considering the joined age-mass PDF at 2 distinct slices of extinction, before integrating over all A_V as in panel (c). We first consider a slice a zero extinction, which is close to the best fit extinction of 0.3. We represent this PDF in green on panel (d) and the corresponding green isochrone on panel (b). We also show a slice at high extinction ($A_V = 2.0$) represented in red with also a corresponding red isochrone on panel (b). This latter slice contains a very small fraction of the complete PDF, but has been renormalized to allow it to be visible in panel (d).

Figure 2 also demonstrates the subtleties in interpreting PDFs. First, the best value does not always correspond to the peak in a marginalized PDF. The dotted lines indicate the position of the best fit in the age-mass-$\mathrm{A_V}$ space, *i.e.*, of the triplet that maximizes the posterior distribution in the full parameter space. Although very close to the peak of the age-mass distribution in panel (c), the best fit suggests a slightly younger and more massive cluster. Second, distributions are complex. The strong correlation between all the different parameters leads to distributions far from Gaussian and sometimes multi-modal.

From this analysis of the integrated light of this particular cluster in the PHAT sample, we obtain a qualitatively good fit, according to the CMD locus of the blue isochrone on panel (b). This panel suggests that the fit indeed accounts for the presence of 2 bright red stars, a significant number of bright main sequence stars, and a reddened main sequence. We also expect that the extended distribution towards younger ages (see Fig 2.d) captures the presence of the two brightest stars on the CMD.

3.3. *Catalog*

Appendix A gives a table of individual estimates for each cluster of the sample, for the discrete models (including continuous extension at the higher mass end). The quoted values in this table are the age-mass-extinction triplets that maximize the posterior probability over the full parameter space. Quoted uncertainties are based on the percentiles of the posterior distribution.

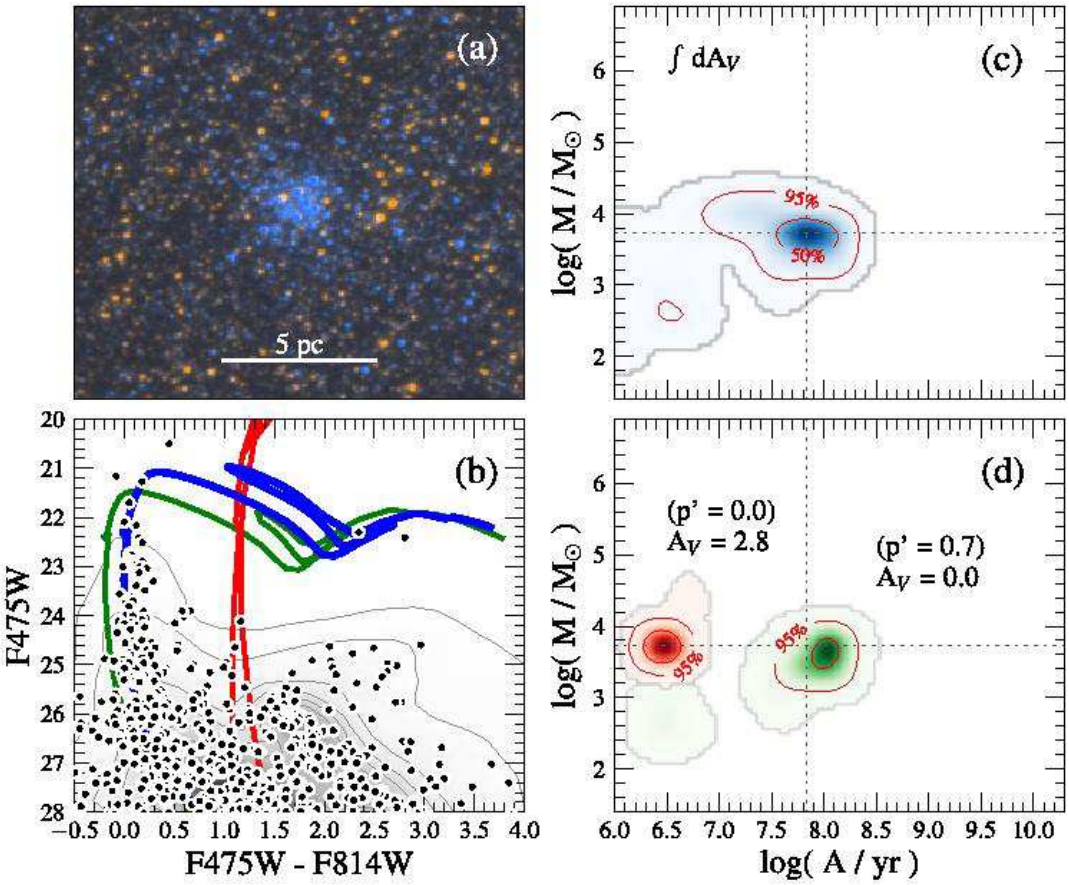

FIG. 2.— Illustration of the estimated age-mass posterior distribution for a given cluster in the PHAT sample and comparison with its color-magnitude diagram (*c.f.*, § 3.2). From top to bottom, and left to right: **(a)** Composite image of optical HST observations of a typical cluster in the sample; **(b)** Color Magnitude diagram of the cluster using PHAT photometry and isochrones based on the color-coded best fits shown in panels (c) and (d). Black dots represent the colors and magnitudes of individual stars in the photometric aperture centered on the cluster. The grey density and contours show the background population distribution in the color-magnitude space, allowing a quantitative estimate of the stellar membership; **(c):** This panel represents the age−mass posterior distribution of this particular cluster while accounting for the full range of allowed extinction values (marginalized over A_V). Contours follow the same definition as in the lower right panel. We obtain a complex distribution in which the most probable value is the triplet: $\{ A_V : 0.3 ; \log(A) : 7.8 ; \log(M) : 3.7 \}$, of which a projection is indicated by the dotted lines on the right hand side panels; **(d)** illustrative representation of posterior distributions for two slices in the extinction dimension, $A_V = 0$ in green and $A_V = 2.8$ in red (distributions are thus independently normalized). The two most likely age-mass-av triplets lead to the green and red isochrones on the bottom-left panel. For each posterior, contours indicate limits at which a given fraction of the distribution is enclosed: red contours indicate 50% and 95%, and a grey contour 99.9% and $p\prime$ the respective probability ratio to the best fit.

As we mentioned above, only the full posterior distribution keeps the complexity of the information. While PDFs from this preliminary study are available upon request, full PDFs will be made available with the cluster catalog when the survey will be completed.

We characterized the potential artifacts and biases in the determination of cluster ages, masses, and extinctions using samples from the synthetic cluster collection. Briefly, for a sample of synthetic clusters spanning the full range of cluster ages, masses and extinctions, we generated 6-filter photometry for one sample of synthetic clusters, and perturbed the "measured magnitudes" according to uncertainties distributed as in the actual PHAT cluster data. We then re-derived the properties for this synthetic set of clusters, and compare the recovered values to the input values.

Overall, we do not find significant age or mass biases from the analysis of synthetic data. The dispersions we obtain are ∼0.14 dex in mass and ∼0.18 dex in age. Those dispersions are consistent with the scatter expected on the basis of the derived PDFs. Based on these tests, we will not venture to interpret features smaller than 0.2 dex in either age or mass (conservatively, since the test dataset corresponds to perfectly modeled data). To reflect these limitations, we bin the posterior probability distributions to 0.2 dex in all the subsequent figures.

We find that large errors in age occur for a few percent of the different realizations of the synthetic clusters, mostly at ages of one or a few Gyr. These errors are due to the age–extinction degeneracy, coupled with the addition of the metallicity as a new parameter for the high mass regime. However these failures can easily be detected through a visual inspection of the color-magnitude diagrams (CMDs). Therefore, we used panel (b) in Fig. 2 as our baseline to visually inspected the CMDs of each observed cluster and added a caution flag in Table 2 when we estimate a potential failure of the fit. These cases include ∼ 60 clusters, mainly in the bulge. In further studies, we will include independent determinations of

the extinction and/or metallicity when available, providing a better set of initial priors.

3.4. *Comparison with color-magnitude diagram analysis*

In this present study, we estimate ages and masses by analyzing the integrated photometry measurements of the clusters. We could argue that such method is uncertain and may not give accurate estimates, especially when the energy distributions of the clusters are deeply affected by stochasticity and stars in rare evolutionary phases with unusual colors. Although limited to nearby galaxies, where clusters can be resolved into stars, the analysis of CMDs offers more robust estimates.

Taking advantage of the high-resolution HST imaging, PHAT provides individual star photometry for a significant number of clusters. To verify the ages and masses obtained from integrated light, we conducted a CMD analysis of 100 clusters. This CMD analysis will be presented in detail in Beerman et al. *in prep*; we briefly summarize the method here. The analysis method is based on Dolphin (2002), which optimizes the likelihood of the observed CMDs with theoretical ones created from stellar evolution tracks, or isochrones, for a variety of ages, mass functions, binary fractions, metallicity, etc., including all observed errors and contamination from a background field population. We selected the sample of 100 clusters for the CMD analysis from various regions of the survey, selecting only clusters with a visible main sequence to ensure the accuracy of the recovered ages. we include clusters from Because of these choices, we restricted the CMD models to have ages less than 10^9 yr.

Figure 3 presents a one-to-one comparison of age estimates derived from integrated photometry (*i.e.*, this present study) with estimates derived from the CMD analysis. Ellipses are located centered on the best fit values and their sizes encode the uncertainties from the CMD and integrated light analyses, respectively. While both methods have their own caveats and failure regimes, in general, the CMD fits have smaller uncertainties. Our choice to limit fits to ages younger than 10^9 yr, is likely to be responsible for the few massive and old outliers. Estimated ages are in agreement within the uncertainties. The dispersion around the 1:1 line is symmetric, suggesting that integrated light estimates do not present any significant bias toward younger or older estimates relative to the CMD derived estimates.

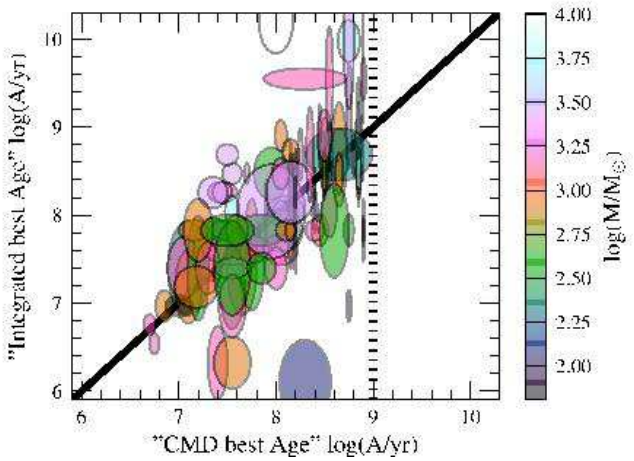

Fig. 3.— Comparison of age estimates from this present work with color-magnitude based estimates for a 100 clusters with visible main sequence. The horizontal axis shows the best age estimates from CMD analysis using MATCH (Dolphin 2002), and the vertical axis represents the best fit values from this present study. Each ellipse represents the uncertainty ellipse of the cluster point, and the colors encode the mass of the cluster. The dotted line is the limit in age imposed during the fitting procedure of the CMDs and the solid line indicates the identity function. This figure shows a broad agreement of both methods within their respective uncertainties.

4. YEAR 1 PHAT CLUSTERS PROPERTIES

The current PHAT cluster catalog focuses on the bulge and three major star forming regions. In this section, we thus look at the first glimpse of what can be expected from the full balance of the PHAT stellar cluster survey, which will include many more clusters and will sample a wider range of environment.

4.1. *Global picture*

In Figure 4, we compare the loci of the observations with a set of unreddened discrete models, in four projections of color-magnitude space. The data are shown together with half of the unreddened models described in § 3.1, which will be used to assign age, mass, and extinction estimates to each individual cluster. These panels illustrate the dispersions in color and flux that results from the stochasticity inherent to the discrete nature of the IMF. Models cover broad regions of the diagrams and complex overlap between ages exist and may not be easily visible at first sight. This complexity will only increases with the inclusion of reddened models. Moreover, even though the models plotted in Figure 4 do not include reddening, the majority of the observed clusters lie well within the regions covered by the synthetic clusters. In contrast, continuous population synthesis models (shown by solid lines) are unable to reproduce some of the observations, even when possible reddening is considered. For example, the top left panel of Fig. 4 shows a significant fraction of robust measurements (black dots) lying on the left side of the continuous age sequence, *i.e.*, the solid line. Allowing for extinction will not help the continuous models to predict such colors. These colors correspond to those expected for relatively low-mass clusters (< a few 10^4 $M_\odot$) that lack any post-main sequence stars.

However, there are also observations even bluer than any models in the F475W−F814W color, lying outside both models range of predicted colors and fluxes. We have colored all points with large photometric uncertainties (> 0.4 mag) with grey, which shows that these outliers are likely to be due to photometric errors. The UV in particular, F275W and F336W, may still be adversely affected by cosmic ray artifacts as cautioned in Johnson et al. (2012).

The locations of the clusters in color and magnitude space draw the unsurprising picture of a cluster population spanning a wide range of age and mass. The entire length of the age sequence seems to be populated and the mass range suggests the presence of a significant number of clusters with masses well below 10^3 $M_\odot$. The two bottom panels reveal a general trend that the most luminous clusters in this sample have old ages; these very old clusters fall above the 10^5 $M_\odot$ curve, and are very likely to

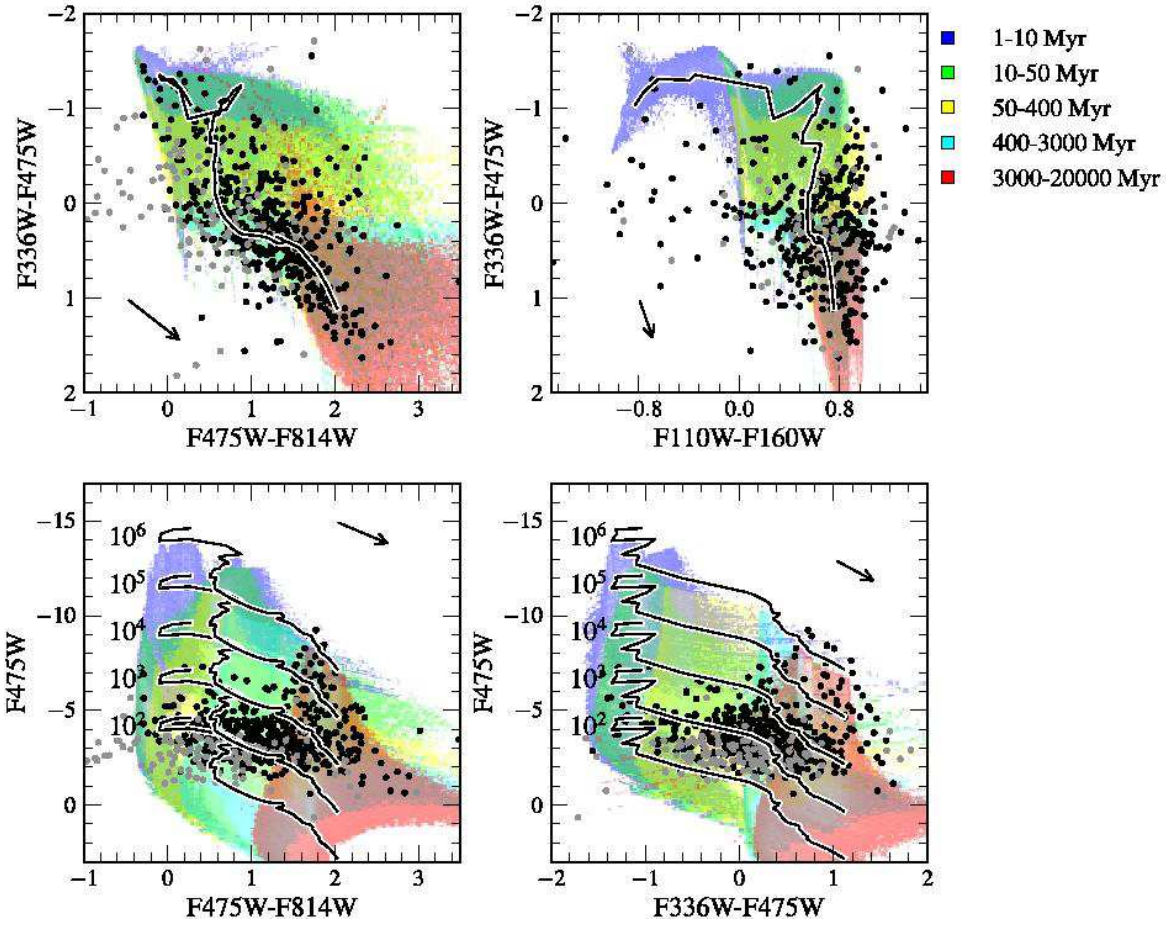

FIG. 4.— Color-color (top row) and color-magnitude (bottom row) location of star clusters with different ages and masses. The black and gray points shows the measured colors and absolute magnitudes of the observed cluster sample. The black points represent optical color uncertainties ≤ 0.4 magnitudes and the gray points uncertainties > 0.4 magnitudes. Unreddened model cluster locations are shown as points whose color encodes age (see right hand side), drawn from the model population described in § 3.1. The solid lines show the predictions from "continuous" population synthesis models for clusters masses of 10^2, 10^3, 10^4, 10^5, and 10^6 $M_\odot$, respectively. Colored dots represent 50% of the discrete clusters available in the Monte-Carlo collection. As the models are not reddened in any panel, but the data presumably are, the extinction vector of $A_V = 1$ is shown for reference. Magnitudes are in the Vega system, in the PHAT ACS and WFC3 filters. The bottom left panel suggests a cluster completeness limit of F475W > -3.

be old globular clusters. The typical completeness limit of -3 in the F475W band is manifested as the lower limit to the data in the bottom left panel.

Figure 5 shows the age-mass-extinction distributions resulting from the analysis described in §3. Each panel on the left hand side represents the joint probability distribution of two of the variables, after marginalizing over the third. The right panels indicate the best fit values and their *relative* accuracy; the ellipses are arbitrarily normalized to reduce the clutter in the figures. The derived ages are distributed between a few Myr and about 10 Gyr, with the few massive candidates appearing only for ages older than 5 Gyr, as expected for the globular cluster population. The derived masses range from a little above the lower limit of our model catalog (50 $M_\odot$) to a bit more than 10^6 $M_\odot$.

The significant number of clusters found to have masses below 10^4 $M_\odot$ is a strong argument against using traditional continuous models that ignore the discrete nature of the IMF. Multiple studies have shown the impact of stochasticity on the determination of ages and masses of clusters (e.g. Barbaro & Bertelli 1977; Bruzual & Charlot 2003; Cerviño & Luridiana 2004; Maíz Apellániz 2009; Piskunov et al. 2009; Fouesneau & Lançon 2010; Popescu & Hanson 2010). In particular they identify artifacts that translate into unphysical overdensities at particular ages for young and old clusters, while underestimating the number of moderate age clusters. These artifacts of continuous models are not present in our analysis (right panels of Fig. 5), for instance we do not predict an accumulation of clusters at young ages and instead a relatively smooth age distribution.

Figure 5 shows almost no old and low mass clusters, nor highly reddened massive old clusters. At old ages, we do not expect many highly reddened clusters to be present, since they should have drifted far from their birth sites. However, even unreddened old clusters are unlikely to be detected unless they were very massive, given that less massive clusters would have faded below the detection limit of the sample. Cluster disruption processes further lower the number of old clusters. Both arguments explain the lack of old, low-mass clusters in the top panel of Fig. 5.

There are poor constraints on the number of clusters

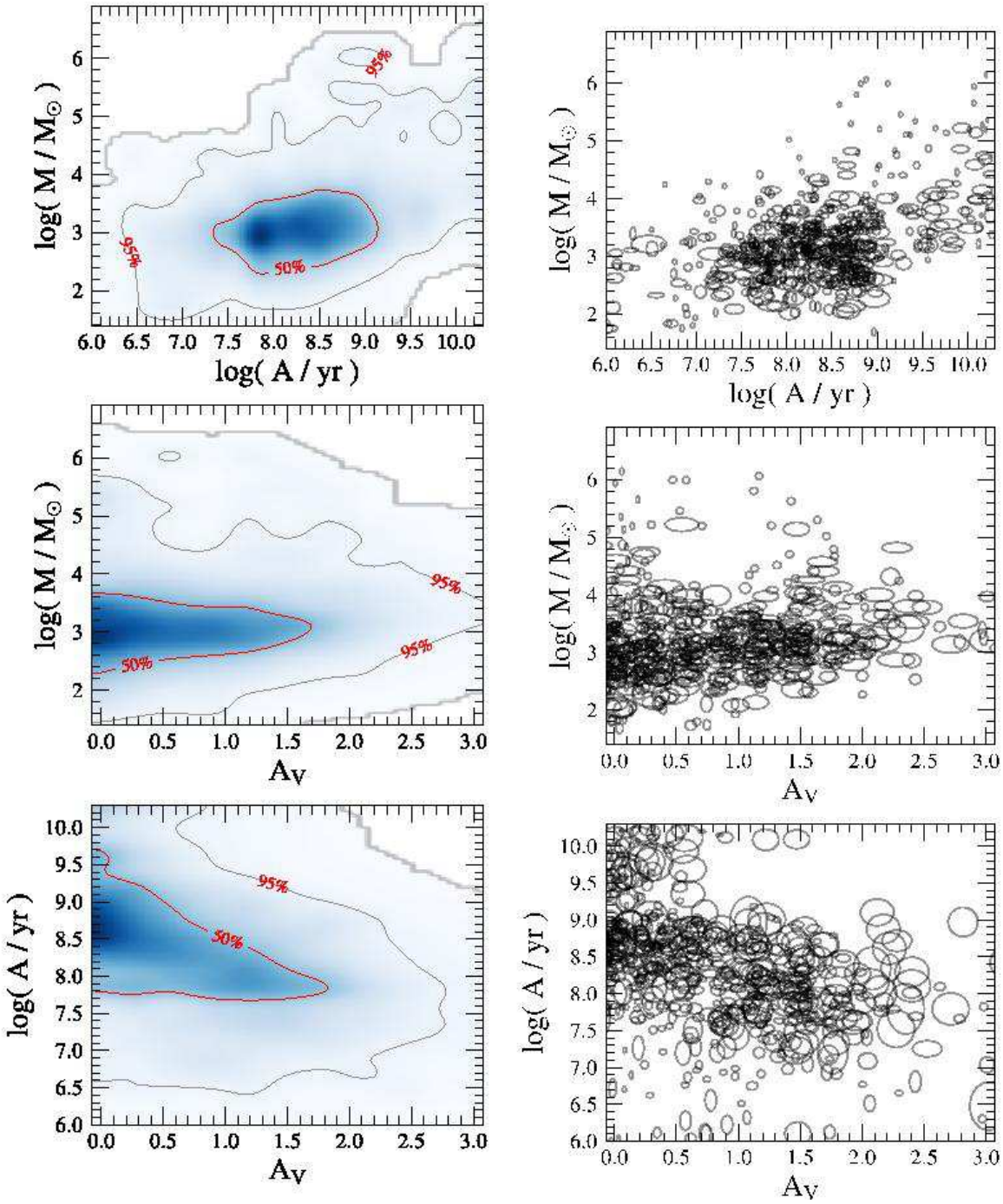

FIG. 5.— Ensemble probability distributions for age ("A"), mass ("M") and extinction ("A_V") of all the clusters. Each panel on the left represents a distribution marginalized over the third parameter and color coded according to the scale on the right side of each panel. Red contours represent the 5%, 50%, and 95% quantiles of the distributions in their respective 2D-space. The gray contour represents 99.9% of the joint distribution. Panels on the right represent the locations of the best estimates, where each ellipse encodes the relative uncertainties of the individual clusters (an arbitrary normalization factor was applied for clarity).

at the high-mass end, mainly due to their low birthrates. If we suppose the canonical power-law with a -2 index, a cluster of 10^5 $M_\odot$ is 100 times less likely to form than a cluster of 10^4 $M_\odot$. Although a large galaxy like M31 may have formed a few dozen clusters above 10^5 $M_\odot$, they are intrinsically rare. Given that we expect to observe all the young massive clusters in the galaxy, the lack of clusters younger than 50 Myr compared to older ages (> 1 Gyr) in the age-mass distribution suggests that M31 may have been more efficient at producing massive clusters in the past. We discuss the decrease in the rate of massive cluster production in more detail in §4.2.

The bottom panel of Fig. 5 shows that very young clusters come with a large range of extinction values, as has been seen in many star forming galaxies (e.g., Whitmore & Zhang 2002; Kim et al. 2012). However, at ages older than 10^8 yr, clusters with more than one magnitude of

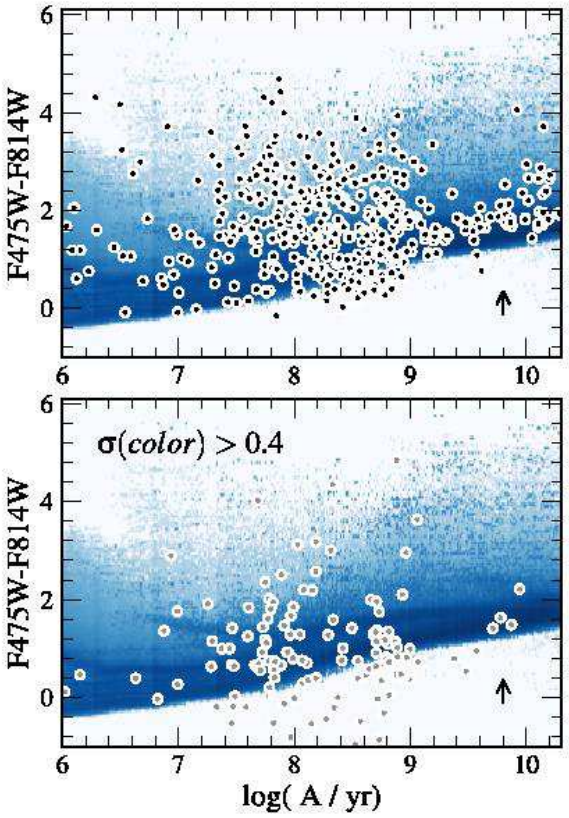

FIG. 6.— Comparison of the cluster optical colors with the estimated ages from our study. The density map in the background represents the sample of (unreddened) models as shown in Fig. 4. One magnitude of extinction A_V translates into a variation of 0.69 magnitude in the optical color indicated by the arrow in the bottom right corner. Each point on this figure represents a cluster from our catalog that we corrected for reddening by applying their respective best fit A_V values. The top panel only shows clusters for which uncertainties in the photometric measurements are smaller than 0.4 magnitudes, whereas the bottom panel only displays the clusters with larger photometric uncertainties. As a result, we show that most of the clusters bluer than the region covered by the models have significantly larger color uncertainties. Clusters are corrected for reddening using their best fit values.

extinction become rare. Between 10^7 and 10^8 yr, the absence of reddened clusters most likely reflects a real lack of highly reddened objects, rather than selection effects, given that the detection limits of the data would allow us to detect 5×10^7 yr old clusters with up to more than 2 magnitudes of extinction, for masses above $\log(M/M_\odot) \approx 4$.

Figure 6 shows the inferred dereddened optical colors of the clusters in the sample. These colors are generated by dereddening the clusters according to their best extinction estimate at their best age (and mass) estimates. This two panel figure distinguishes clusters with typical photometric errors (top panel) from the ones with abnormally large uncertainties, due primarily to uncertainties in background determinations. In both plots we indicate the color-age space covered by the models in blue. The comparison between observations and best fit values from our models confirm the self-consistency of the analysis: clusters find logical estimates when uncertainties are typical (top panel), while large uncertainties may result in unsatisfactory estimates (bottom panel).

4.2. *Age distribution of the clusters*

The age probability distribution represents the apparent age distribution of the clusters, resulting from the combined underlying cluster formation history, the cluster destruction rate, and observational selection effects. The distinction between the observed age distribution and the history of the cluster formation rate is analogous to the difference between the present day and the initial mass function.

We can derive the age distribution of the ensemble cluster population. In principle, we derive this distribution by optimizing our prior age distribution leading to a more complex framework that we will further develop in the context of cluster disruption. In the context of this present work, we approximate this distribution with the co-add of the age probability distribution functions (PDFs) of each individual cluster. This procedure tends to increase the presence of tails in the distributions, however it produces a more accurate global age distribution than assigning each cluster to a single "best-fit" age, especially in the light of complex and often multi-modal PDFs. The combination of PDFs also preserves the relative quality of the fits between clusters. Moreover, probability distributions are more robust to binning effects.

The composite distribution of ages for the ensemble of clusters is shown in Fig. 7 (black solid line). This figure shows two representations of the age distribution of the ensemble of clusters using both PDF representations as a function of logarithmic age. These probability distributions show the relative number of clusters (not mass in clusters) as a function of age. The top panel shows the probability distribution of logarithmic ages, $dN/dlog(A)$, in contrast with the bottom panel showing the distribution of age, dN/dA; $\mathcal{P}(\log(A))$ is defined such that the average number of stars in a given logarithmic interval $[\log(A), \log(A)+d\log(A)]$ is $dN = N\,\mathcal{P}(\log(A))\,d\log(A)$, while $\mathcal{P}(A)$ is defined such that the average number of stars found in the linear age interval $[A, A + dA]$ is $dN = N\,\mathcal{P}(A)\,dA$. Hence an equal number of clusters at every age would appear as a constant horizontal line in the bottom panel and as an exponential function in the top one. In both representations we also include dotted lines showing the composite distributions when restricted to masses above 10^3 $M_\odot$, the estimated completeness limit of our sample over at least a few 100 Myr.

The uncertainties in the age distribution (represented by the shaded region on Fig. 7) are dominated by the random sampling of a finite number of a relatively small ($\sim$ 600) sample of clusters. At old ages (e.g., 5 Gyr) where there are few clusters, including or removing a single cluster will lead to large variations. In contrast, such an alteration of the sample at 100 Myr will have less influence. To estimate these sampling uncertainties, we characterize the variations of the posterior distributions by bootstrapping (Efron 1987; Rubin 1981). Specifically, we make 1000 realizations of the cluster sample, randomly drawing 601 clusters for each but allowing duplications, and re-derive the ensemble age distribution for each realization. The shaded region indicates the range containing 95% of the realizations of the age posterior distribution. Each individual realization is also used to further assess uncertainties when comparing different cluster age distribution models.

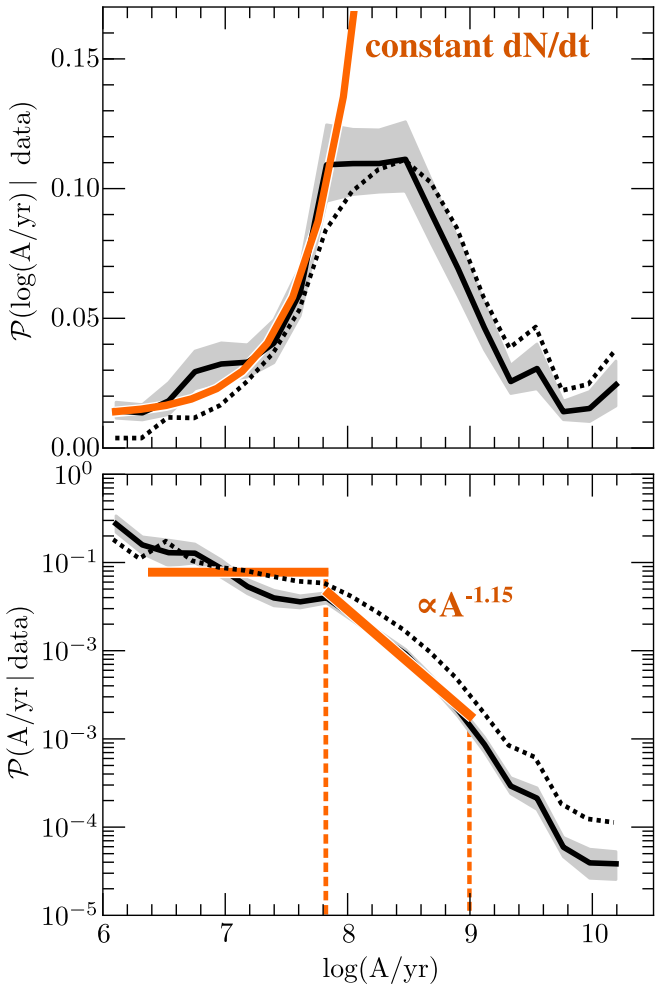

Fig. 7.— Age distribution (marginalized over mass and extinction) of the entire sample regardless of the positions of the clusters. Thick black lines represent the total distribution while shaded regions are their respective uncertainties based on bootstrapping the cluster sample as described in the text (§4.2). The orange thick line on the top panel represents a constant number of clusters, over the last 100 Myr. It corresponds to the horizontal line on the bottom panel. To the latter, we have also added the best fit described in §4.2. Also shown of both panels, a dotted line corresponds to the age distribution restricted to masses above 10^3 $M_\odot$, where effects of observational completeness are limited.

The distribution in Fig. 7 shows that the present day ages of clusters span from a few Myr up to 10 Gyr. The young cluster age distribution (< 100 Myr) is relatively flat. Although we note a small decay, the age distribution is statistically consistent with a uniform distribution over the last 100 Myr, as indicated by the thick orange line. If the birth rate of clusters has been relatively steady over this same interval, then the nearly constant age distribution suggests that the cluster disruption processes are likely to be inefficient over $\sim$ 100 Myr timescales. We revisit this point fully in §5.2. If we apply a mass cut at 10^3 $M_\odot$, at the expected mass completeness limit, the resulting cluster age distribution (dotted line in Fig. 7) show a better agreement with a constant rate at younger ages and little change at older ages.

The distribution drops off at ages older than 10^8 yr, as expected from cluster disruption and observational selection limits (as described in §4.1). We fit a power-law

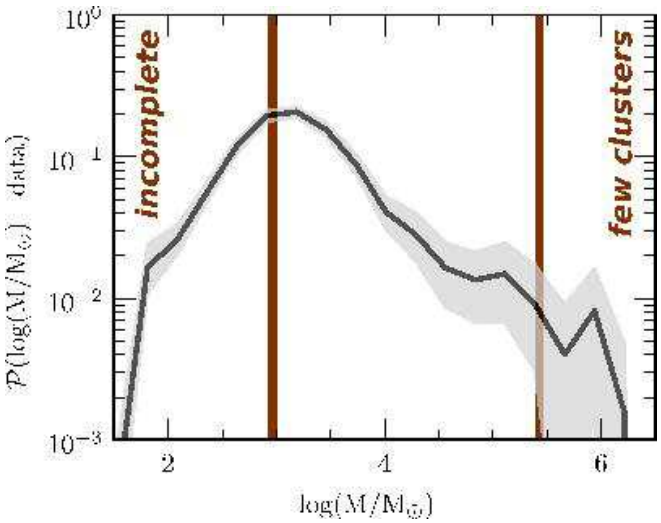

Fig. 8.— Mass distribution (marginalized over age and extinction) of the entire sample regardless of the positions of the clusters. Thick lines the total distribution while shaded regions are their respective uncertainties based of bootstrapping the cluster sample as described in the text (§4.2). The two vertical lines represent the regime limits where the distribution is less than 50%-complete (left) and stochastic presence of clusters in our sample is dominant: uncertainties are more than 50% of the value (right).

with spectral index β to the observed age distribution for ages between 10^8 and 10^9 yr, using a χ^2 likelihood statistics:

$$\mathcal{P}(A/yr) \propto A^{\beta}. \quad (4)$$

We find that the observed present day age distribution in this interval can be approximated with a power-law of index $\beta = -1.15 \pm 0.1$. However, note that this power-law does not map directly into the cluster formation rate since no cuts have been applied to ensure that the same range of cluster masses is detectable at all ages. The distribution of ages in the older regime is consistent with observations of other galaxies the literature (e.g., Hunter et al. 2003; de Grijs & Anders 2006; Chandar et al. 2010; Bastian et al. 2012; Fouesneau et al. 2012), which also find power-law present day age distributions with spectral indexes close to -1.

4.3. *Mass distribution of the clusters*

The marginal distribution of cluster masses (*i.e.*, the distribution summed over all ages and extinctions) is shown in Fig. 8. We derived the composite distribution of the whole cluster sample from their individual probability distributions as it was done for the age distribution in §4.2. The resulting mass distribution is uncertain in the low-mass end ($\sim 10^3$ $M_\odot$), where the sample is less than 50%-complete. We adopt this limit as a lower mass limit for this distribution. There are also significant uncertainties in the high-mass regime, where the rare presence of one single massive cluster can induce large variations in the distribution. To minimize stochastic sampling of the cluster mass function, we conservatively define a mass upper limit as the mass where the uncertainties calculated from bootstrap resampling (*cf.* §4.2) are more than 50% of the median value. The mass function is most reliable between these two regimes, which are delimited by the thick vertical lines in Fig. 8.

Over the interval of $10^3 - 10^{5.5}$ $M_\odot$, the observed

present day distribution of masses for the entire sample can be approximated by a power-law,

$$\mathcal{P}(M/\ \mathrm{M}_\odot) \propto M^\alpha, \quad (5)$$

with index $\alpha = -1.73 \pm 0.11$. Alternatively, if we restrict the sample to only clusters with ages between $10^7 - 10^9$ yr in order to avoid possible incompleteness, the distribution becomes steeper with an index of -1.89 ± 0.12, over the same mass range, but remains statistically compatible with the fit of the full distribution. Overall, we find that the present day cluster mass function is well-described by a power-law, which agrees well with previous analyses of other galaxies (e.g., in Fig. 10 of the review from Portegies Zwart et al. 2010). In particular we find that the younger (< 1 Gyr) cluster mass distribution is a close match to a power-law distribution with spectral index −2, in agreements with several other cluster mass function determinations that find indices close to −2 (e.g. Zhang & Fall 1999; McCrady & Graham 2007; Bik et al. 2003; Chandar et al. 2010; Popescu et al. 2012). Variation from the canonical −2 index of the present day mass function may be the result of stochastic formation of the cluster population, in which a variation of one massive cluster could induce such variation. Variations may also be the result of systematics that we explore in Section 5.

The mass distribution has an apparent peak near 10^3 $\mathrm{M}_\odot$, which falls off towards lower masses. Based on the Monte-Carlo collection, we know that $\log(M/\ \mathrm{M}_\odot) = 3.1$ is the threshold mass under which more than half of the clusters have fluxes below the 50%-completeness limit (defined in §2) in the F475W photometric passband. This peak is therefore more likely to be due to the incompleteness of the cluster sample at low fluxes, than a real feature in the cluster mass distribution. The exact characterization of this peak is uncertain, because: (i) being faint, the low mass objects have larger observational errors than massive ones; (ii) clusters that have low masses while remaining above the detection limits must be young, and therefore are in the regime most sensitive to the stochastically sampled cluster models; and (iii) the detection of such low mass clusters becomes inefficient due to their low contrast against the field star background.

4.4. *Environmental Variations*

The present day age and mass distributions discussed in §4.2 and 4.3 were derived for the sample as a whole. They therefore include clusters in the bulge (B01), which has a distinct cluster population observed with a different detection efficiency. In this section we explore potential variations in distributions of cluster properties at different positions within the galaxy to make a first assessment of environmental dependencies in the cluster population.

Figure 9 shows the 2-D joint parameter distributions for each of the bricks (*i.e.*, equivalent to Figure 5, but subdivided by regions). Figure 9 highlights the variable completeness of our sample across the galaxy; indeed, it is very difficult to detect low-mass and/or highly extinguished clusters in the bulge, because of the high luminosity background. In contrast, it becomes straightforward to find them in the outer the disk. From the four top panels of Fig. 9, one can see that the effective 95% completeness moves ∼ 1 dex in both age and mass, such that older and lower-mass objects are more easily detected at larger radii. This effect is reflected in the translation to the left of the diagonal limit in the bottom right corner of the upper row of the plots.

Figure 9 shows that the difference between the bulge and the other regions is very strong. Most of the massive old clusters are in the bulge, making up the bulk of the globular clusters from our sample. In contrast, the lowest-mass clusters are mainly in the outer regions of M31 (B15 and B21), which have the lowest stellar background density, and thus the best contrast for detecting low-luminosity clusters. Moreover, all of the disk fields are quite similar, beyond the small variations in sensitivity. As a result, for the rest of this paper will consider only the disk fields (B09, B15, and B21).

Figure 10 compares the marginalized age and mass distributions for each of the three disk regions, following the same conventions as Figs. 7 and 8. The black line reproduces the distribution of the whole sample, for reference. There are roughly twice as many clusters in B15 relative to the two other regions, leading to larger uncertainties in the inner (B09) and outer (B21) regions.

Age distributions— The top panel of Figure 10 shows that there are no significant radial changes in the local age distributions, when average over the scale of the PHAT bricks (1.5×3 kpc at the distance of M31). We can see this similarity more clearly in Fig. 11, where we overlay the present day age distribution for all 3 disk regions.

At young ages (< 100 Myr), all three age distributions are consistent with a uniform distribution over the last 100 Myr suggesting that any variations in the cluster formation rate were coherent over the galaxy.

At older ages (> 100 Myr), the age distributions in B09, B15, and B21 are all compatible with a power-law. The power-law spectral indices of the age distributions from 10^8 to 10^9 yr in Fig. 10 are -1.39 ± 0.1,-1.11 ± 0.1, and -1.21 ± 0.1, for Bricks 9, 15, and 21, respectively, which can be compared to the power-law of index -1.15 ± 0.1 derived for the whole sample (§4.2). The broad similarity among the age distributions (illustrated in Figure 11 by the orange shaded region) suggests a common cluster formation history within the three different forming regions. In other words, the net result of changes in the cluster formation rate and destruction rate were coherent across the galaxy, in spite of the fact that the disk cluster sample spans a broad range of environments. In particular, we would have expected that variations in the local gas density should lead to different cluster disruption efficiencies (Boutloukos & Lamers 2003; Lamers et al. 2005). However we do not observe statistically significant differences in the age distributions of clusters from the ring (B15) and the most outer-region (B21), where the gas density is the highest and the lowest, respectively. Note that this spatially resolved analysis suggests that the slight deviation from consistency with Fig. 7 was primarily due to the inclusion of clusters in the bulge field.

Unfortunately, the current data are not sufficient to distinguish statistically significant variations from brick to brick. While there is a hint of a radial variation in the position of the roll-over of the distribution, a reliable

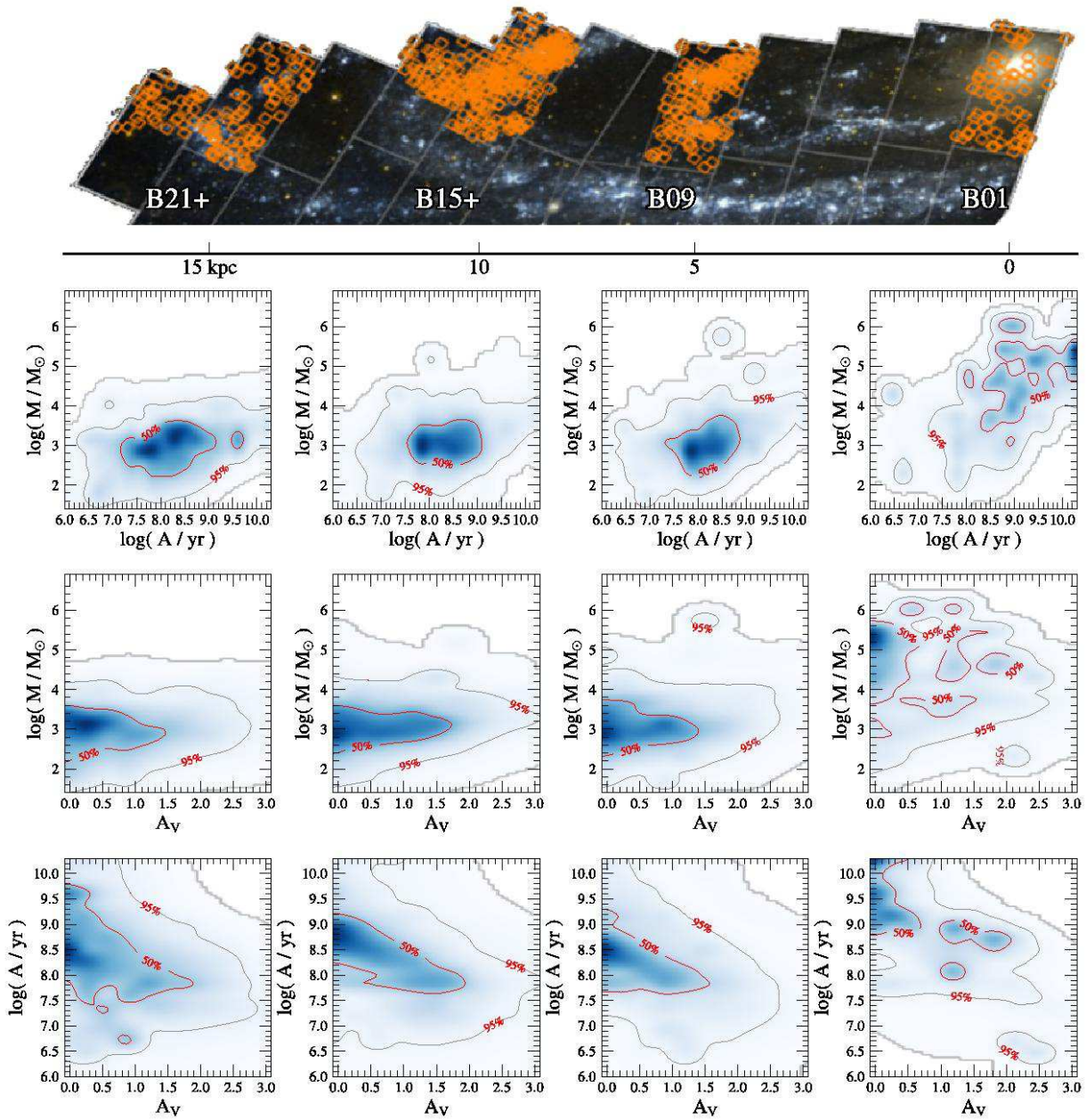

Fig. 9.— Cluster mass, age and extinction distributions in different radial distance regimes in M31. The panels in the bottom three rows show different 2-D projections of the joint Age-Mass-Extinction ($A-M-A_V$) posterior distribution. Each column represents one of four different sub-regions of M31 (shown on top row, with four clumps of cluster positions at B21+, B15+, B09 and B01, left to right columns, respectively). These are analogs of Fig. 5, which shows the equivalent distributions summed over the entire sample. Apart the bulge, other regions exhibit similar distributions with possible completeness variations.

interpretation of the roll-over is difficult without larger samples and a better characterization of the effects of the completeness of the sample. We therefore postpone this analysis to the full PHAT dataset.

Mass distributions— The bottom panels of Fig. 10 show the mass distributions of all clusters in the 3 disk fields. The shaded regions follow the same conventions as in Fig. 8. The lower-mass regime is defined to be the region where the sample is less than 50% complete (*i.e.*, $M < 10^{3.3}$ M$_\odot$). By excluding this mass region, we remove sensitivity and ensure that we have the same high completeness in all three disk regions. We also set an upper mass limit to be where the uncertainties are more than 50% of the median value (as explained in §4.3). The upper mass limit is very different in the 10 kpc star forming ring (B15) due to the presence of more massive clusters than in the two other regions (B09 and B21). This difference is primarily due to the factor of 2 to 3 larger in the number of clusters in Brick 15. For stochastic sampling of the low-frequency tail of a power-law distribution, the number of massive clusters in each region is expected to vary much more than this factor of $2-3$, and instead should vary by up to a factor of 10 (see Table 1). In other words, while B15 has a greater number of massive clusters, it still has fewer than we would expect

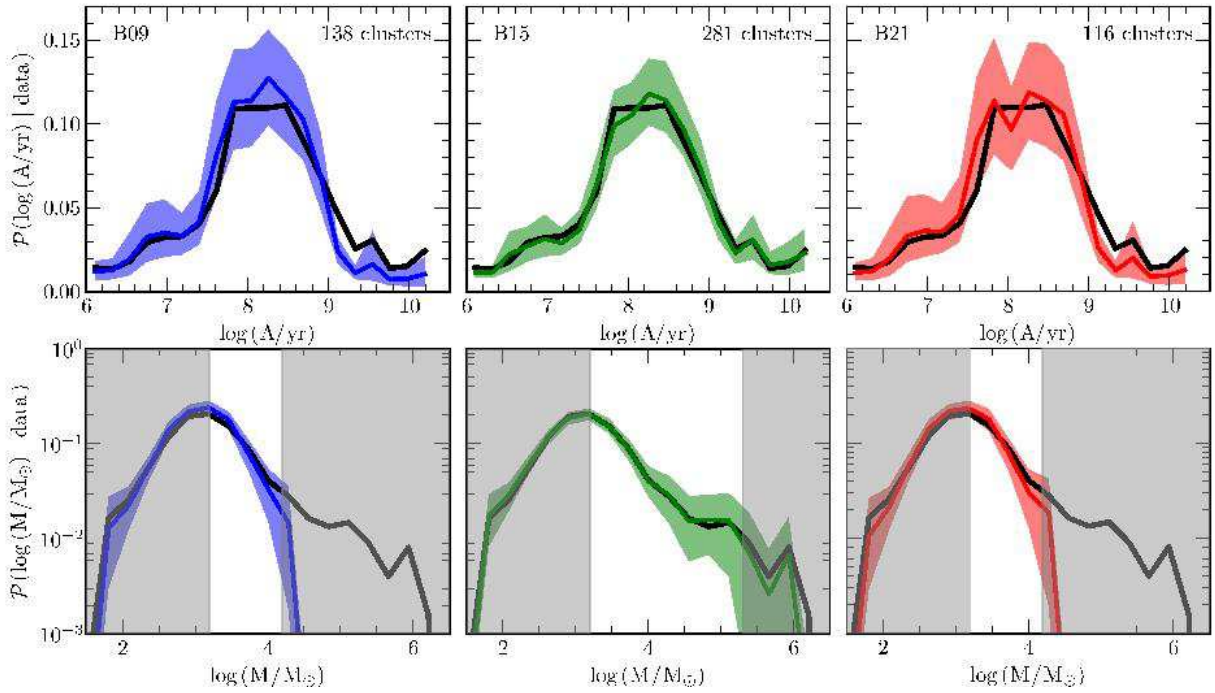

FIG. 10.— The individual marginalized probability distributions for age (top row) and mass (bottom row), for clusters in Bricks 9, 15+, and 21+ (left to right, respectively) Each column represents the distributions derived within a single brick. Shaded colored regions indicate the uncertainties in the distributions, derived from bootstrap re-sampling. For reference, the black lines show the distribution derived for the entire sample (e.g., Figs. 7 & 8). Gray shaded regions on the mass plots indicate regions where either completeness (left shading) or stochastic sampling of the massive clusters (right shading) are dominating the distributions. These regions are not included when fitting the distributions with power-laws.

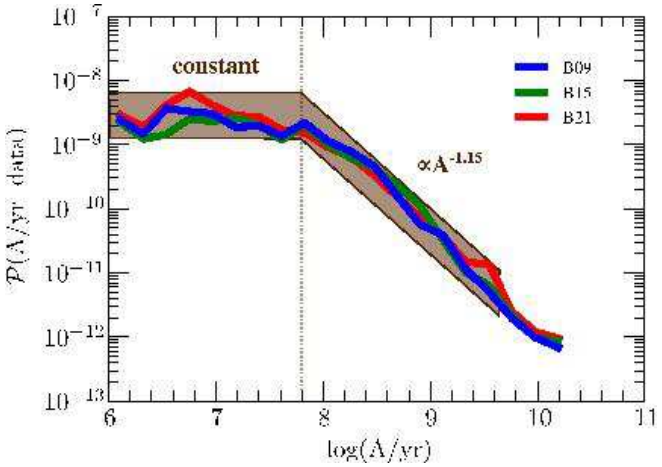

FIG. 11.— Distributions of cluster ages per linear age bins as a function of log(age) for each individual brick. This corresponds to the bottom panel of Fig. 7 for the clusters in each of the three regions in the disk. The dark shaded region illustrates the cluster age distribution described in §4.4: constant over 100 Myr followed by a power-law decline with index −1.15.

to follow the same mass function. We further discuss the lack of massive clusters in §5.3.

Qualitatively, B09 and B21 share a similar present day mass distribution within the mass range where the estimated distributions are reliable. At first glance, however, the mass distribution in B15 appears to be different, although this difference may partially reflect the much larger mass range that can be probed reliably in Brick 15.

To quantify the differences among the bricks, we have fit each distribution with a power-law distribution. Based upon the bottom row of Fig. 10, a fit to the mass distribution of Brick 15 may be more consistent with the two other regions if we limit the mass interval to a common range. Therefore, we restrict the fits to both the reliable mass ranges (*c.f.* § 4.3) and a common mass range ($3.2 < \log(M/\,M_\odot) < 4.2$), while accounting for their associated uncertainties. We repeat this exercise using bootstrap resampling of the cluster sample in each brick. The top panel of Fig. 12 shows the resulting mass spectral index probability distributions for each individual brick. We obtain broad distributions for α in B09 and B21, as expected from the limited mass range used during the fit and the smaller number of clusters. The dashed green line shows the fit of Brick 15 mass distribution when including the full reliable mass interval, while the solid version shows the resulting distribution when restricting B15 to the same mass range as B09 and B21, of $3.2 < \log(M/\,M_\odot) < 4.2$. We find a relatively narrow distribution for B15 given the large number of clusters, and as expected, limiting the mass interval favors steeper mass functions by ~ 0.2 dex. When fitting over the common mass range, we obtain the following values and standard deviations: B09: -2.2 ± 0.17, B15: -1.8 ± 0.1, and B21:-2.1 ± 0.14 (-2.24 ± 0.1 for the full reliable interval). Although all of the three distributions of α are compatible (within 2-σ) with a single power-law of index of -1.8 (found in §4.3), the differences from this overall description are close to 3-σ.

Given both B09 and B21 share a similar environment and that they also seem to follow a similar age-mass distribution, we combined those samples into a super region probing spiral arms. This combination increases

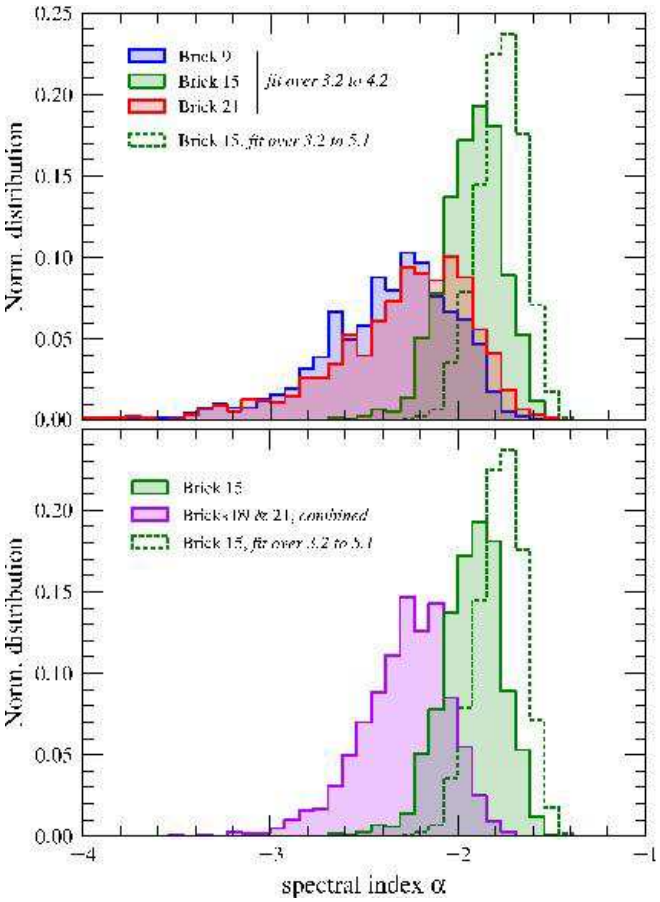

Fig. 12.— The distributions of the spectral indexes recovered from fitting a power-law to the mass distributions of the 3 outer regions in Fig. 10. On the top panel, we show the distributions recovered from fitting over the same mass range: $3.2 \leq \log(M/\ M_\odot) \leq 4.2$. Because they appear similar, on the bottom panel, we grouped Brick 9 and 21 during the fit in order to increase the number of clusters. In both panels, the dotted histogram represents the distribution recovered if one fit the mass distribution of Brick 15 ("10 kpc-ring") up to $\log(M/\ M_\odot) = 5.1$, limit at which uncertainties dominate the mass distribution.

the number of clusters in the statistics allowing us to compare 2 distinct types of star forming regions in M31: spiral arms and the ring. The bottom panel of Fig. 12 compares the distributions for B15 from the top panel to the distribution obtained for the combination of B09 and B21 cluster samples. As expected, the combination of the two regions narrows down the spectral index dispersion. However the resulting distribution does not reconcile with what we find in B15 (best fit of -1.8 ± 0.12), and the resulting discrepancy is statistically increased. As the PHAT survey will eventually cover inter-regions and include many more clusters, we will be able to fully characterize the mass variations with environmental conditions.

5. DISCUSSION

5.1. *Exploration of possible systematics*

We have compared the cluster populations in 3 star forming regions in M31, and may have identified the first clear evidence of variation of the present day cluster mass function within one galaxy. On the other hand, we find very similar age distributions in the same three regions. We now explore the possible observational artifacts that could be affecting our analysis.

Systematics from the analysis method— We have made multiple assumptions when deriving ages and masses for the cluster samples. Some assumptions could potentially lead to systematic errors in the age and mass determinations.

First, we assumed in the models that no ionizing photons escape from the cluster. If some photons do escape, then we will over-estimate the flux in the nebular emission (continuum + lines), and thus, the model colors will vary. These color variations will shift clusters to different apparent ages, with little change in the inferred masses. Moreover, these effects are in the opposite sense of what is needed to explain the data where we find very similar age distributions, but differences in the observed mass functions.

Second, there may be some level of inconsistency between the stellar evolution models and the actual clusters, which could lead to biases in the derived ages and masses. However, such an effect would be apparent in all regions, and would not produce radial variations.

Third, the lower-mass limit of the current collection is sufficiently low that the choice of the stellar IMF or its sampling method can affect the derived SEDs. If real clusters have a stellar mass function different from that assumed, then the cluster ages and masses would be biased. Again this would not produce a radial variation in the mass distribution of the clusters, unless the stellar IMF were also environmentally dependent.

Finally, our choice of priors during the analysis of cluster colors may not be optimal. We assumed uniform expectation in age and mass on logarithmic scales, but our tests have shown that varying the prior assumptions does not significantly affect the resulting distributions. Therefore, our choice of prior is unlikely to to produce variations in the cluster mass distribution across the galaxy.

Apart from an environmental variation of the initial stellar mass function, none of the above possibilities appears likely to produce the observed radial variations in the cluster mass function while keeping similar age distributions. All seem likely to affect all of the regions in a similar manner (outside of the bulge).

Variations in the fraction of bound clusters— Our analysis is based on the cluster sample from the Johnson et al. (2012) catalog. Like any catalog, the resulting sample has biases that reflect how the clusters were selected. Johnson et al. (2012) adopted a definition of a "star cluster" to be a group of stars assumed to form a coeval population (*i.e.*, single age, metallicity, etc.). This definition includes any clustered stars regardless of whether they are gravitationally bound or not. It is therefore possible that the observed variations are due to radial changes in the relative numbers of gravitationally bound clusters and unbound associations. Associations are most likely young because of their intrinsic instability (Gieles & Portegies Zwart 2011). When their size is comparable to stellar clusters, they are also likely to be relatively low mass. Therefore, increasing the proportion of associations will lead to a higher fraction of clusters with young ages and low masses.

However, we do not observe a significant change at

TABLE 1
FIELD PROPERTIES

Brick Name	R_{gal} (kpc)	F475W$_{lim}$ at 50% (1)	N_{cl}	N_{cl} ($M > 10^3$ M$_\odot$)	best β (2)	best α (3)	M_{max} M$_\odot$ (4)
B01	0	-3.8	61	61	–	–	–
B09	6	-3.5	138	70	-1.11 ± 0.1	-2.2 ± 0.17	2.5×10^4
B15	10	-2.8	281	165	-1.21 ± 0.1	-1.8 ± 0.1	1.7×10^5
B21	15	-2.2	116	54	-1.39 ± 0.1	-2.1 ± 0.14	2.0×10^4

(1) 50% Completeness limit in F475W (Johnson et al. 2012),
(2) best age spectral index: $\mathcal{P}(A/\text{ yr}) \propto A^{-\beta}$, with $8 < \log(A/\text{ yr}) \leq 9$ (§4.4),
(3) best mass spectral index $\mathcal{P}(M/\text{ M}_\odot) \propto M^{-\alpha}$, with $3.2 < \log(M/\text{ M}_\odot) \leq 4.2$ (§4.4) ,
(4) maximum expected mass from a power-law with index given by their best β (§5.1).

young ages between the three different regions. Including many low-mass objects could result in a steeper mass function. If there is a systematic radial change in the fraction of associations, we expect this fraction to be the highest in B21, which is the ideal environment for finding faint objects because of its low background and relatively low density of sources and extinction. However, as shown in §4.4, the present day mass function of B21 is similar to that of B09, which is the inner most region used in this comparison. When combined with the fact that we see no obvious variations in the observed age distributions at recent times, it seems highly unlikely that variations in the fraction of bound clusters are systematically affecting the observed age and mass distributions.

Completeness variations and missing low-mass clusters— The completeness of the PHAT cluster sample is a complex function of 6 filters photometry affected by measurement errors, which thus does not translate into a single mass cut in the age-mass plane. Moreover, clusters in this sample are partially resolved into stars, which increases the complexity of estimating the completeness accurately.

From the observational limits given in Johnson et al. (2012), we derived an approximative mass completeness of $\sim 10^3$ M$_\odot$ using our collection of synthetic models.

Instead of deriving a complex completeness function, we instead applied a conservative mass cut of $10^{3.2}$ M$_\odot$, based on combining the observational limits given in Johnson et al. (2012) with our collection of synthetic models. Above this mass, we expect the sample to be essentially 100% complete, except perhaps at the very highest extinctions. This expectation is born out by the distributions in Fig. 9, which show no obvious signs of incompleteness at the $10^{3.2}$ M$_\odot$ level.

Brick 15 is the most gas rich of the 3 star forming regions. It is possible that B15 contains more dust, and this results in higher incompleteness due to dust extinction. We can estimate the number of potentially "missing" clusters in Brick 15 by deriving samples to make an intrinsic mass power-law with index $\alpha = -2$ appear to have a distribution of $\alpha = -1.8$ (as the median value in Brick 15) We find that Brick 15 would need to have a factor of ~ 5 more clusters between 10^3 and 10^5 M$_\odot$ to recover a spectral index of -2. This corresponds to having 20 missing clusters above 10^4 M$_\odot$, that were undetected because of more than 2 magnitudes of extinction. We find this possibility to be unlikely, given that the A_V distribution of detected clusters falls off steadily towards high extinctions. Moreover, we have visually inspected all F160W images for embedded clusters at the locations of dense molecular cloud from high resolution CARMA maps of B15 (Schruba et al., *in prep*) and we find no evidence for highly embedded massive clusters.

5.2. *Age distribution and the cluster formation history*

In this study, we find that the present day cluster age distribution, dN/dt (bottom panel of Fig. 7), is globally flat over the last 100 Myr, particularly where confined to the disk fields (Fig. 11). There are other cluster samples from the literature that show the same constant distribution at young ages (e.g., Lamers et al. 2005, limited to 600 pc from the Solar neighbourhood; Hodge 1987; Chiosi et al. 2006, flat over 1 Gyr in the SMC). After this initial 100 Myr period, we find a power-law drop-off at older ages consistent with index -1.15. This index may change when we eventually include the complete sample from the PHAT survey, which will provide greater weighter of regions that lack recent star formation than the Year 1 Johnson et al. (2012) catalog.

The interpretation of the observed dN/dt distributions is not straightforward, because these distributions are heavily dependent on the observational completeness of the sample, the birth rate of the clusters as a function of time, and the efficiency of the cluster disruption processes as a function of time, mass, and environment. We are therefore deferring a full analysis of the age distribution until a subsequent paper, when we will have a larger number of clusters in the sample and a better characterization of its completeness.

As an intermediate step, however, we can draw an initial comparison between the observed present day age distribution and that expected under a few assumptions. If one assumes that the cluster population formed at a constant rate and with a *power-law initial cluster mass function* (ICMF), and *no dissolution*, Gieles & Bastian (2008) demonstrate that the age distribution can be analytically estimated. Based on continuous population synthesis flux predictions for cluster fading, they show that the observed age distribution should follow a power-law distribution with an index of ~ -0.7, if the sample is limited by one optical band detection, and dN/dt should be constant, if the sample is mass limited.

We find a uniform distribution for the first 100 Myr. If we assume that the young clusters from Johnson et al. (2012) are complete down to our $10^{3.2}$ M$_\odot$ mass limit,

then we should obtain a constant distribution until the age that the fading or disruption starts to remove clusters from the sample.

We find that the drop-off occurs at $\sim$ 100 Myr, independent of the region of the galaxy, suggesting that cluster disruption is little to no effect prior to this timescale. In addition, the 100 Myr extent of the flat dN/dt distribution appears to the same in all regions, suggesting that the environmental dependence of the cluster disruption must be weak.

At older ages ($>$ 100 Myr) we find a power-law decrease in the observed dN/dt distribution, with an index of $\beta = -1.15$. This index is steeper than the predicted value by the cluster fading model of Gieles & Bastian (2008) in the presence of a magnitude limit. This may suggest that there are some cluster disruption effects at work above the $10^{3.2}$ $M_\odot$ mass limit of our analysis. On the other hand, the role of selection effects has not yet been fully qualified and can potentially lead to the steepening that is observed. We will work on this issue more fully in an upcoming paper.

5.3. *Truncated Mass Function*

The reliable mass range over which we can fit the present day mass distribution with a power-law functino varies from one region to another. We adopted different limits motivated by the lack of massive clusters in B09 and B21 in contrast with B15. This difference could simply reflect the smaller number of clusters overall in B09 and B21, or it could reflect that the cluster mass function in these bricks is "truncated", given that other studies have found evidence for a truncation of this power-law at the high-mass end (e.g., Bastian & Gieles 2008; Larsen 2009; Vansevičius et al. 2009, in M31 for the latter). To test for a possible truncation, we can estimate the most-massive cluster we would expect from an untruncated power-law mass function and compare to our observations.

To do this test, we assume that the cluster formation rate is constant and that the cluster mass function follows a power-law mass distribution over a mass range $[M_1, M_2]$,

$$\mathcal{P}(M/\ \mathrm{M}_\odot) \propto M^\alpha, \tag{6}$$

where α the spectral index of the cluster mass function. With these assumptions, we can define the probability of obtaining a cluster with a mass m above a given mass M as

$$\mathcal{P}(m \geq M \mid \alpha) = \frac{\int_M^{M_2} x^\alpha\, dx}{\int_{M_1}^{M_2} x^\alpha\, dx}, \tag{7}$$

We need then to introduce the total number of clusters, N_{cl}, formed from the mass distribution. If we consider independent draws from this mass distribution, then the expected maximum mass M_{max} satisfies the condition that we have one and only one cluster for $m = M_{max}$, therefore:

$$1 = N_{cl} \times \mathcal{P}(m > M_{max} \mid \alpha) \tag{8}$$

$$M_{max} = \left\{ M_2^{\alpha+1} - \frac{1}{N_{cl}} \times \left(M_2^{\alpha+1} - M_1^{\alpha+1} \right) \right\}^{-(\alpha+1)} \tag{9}$$

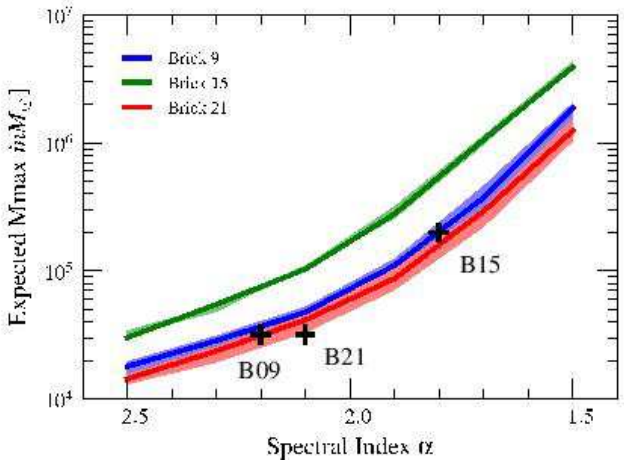

Fig. 13.— Distributions of expected most massive cluster mass as a function of the power-law spectral index, in each of the 3 outer regions of the study. Shaded regions are based upon the Poisson variations of the number of clusters per brick. Black crosses are the mass cut applied during the fit in §4.4 for the labeled regions.

If we consider the upper mass limit M_2 to be infinite (*i.e.*, no truncation), and $\alpha < -1$ for convergence, then:

$$M_{max} = M_1 \times N_{cl}^{\alpha+1} \tag{10}$$

Figure 13 shows the different expected distributions of M_{max} as a function of the power-law index α, for each field brick in our study. The different curves are constructed from Eq. 9, assuming the mass function is defined within $10^3 - 10^7$ $M_\odot$, to match our typical completeness limits. The number of clusters N_{cl} above 10^3 $M_\odot$ is taken from Table 1 for each region. We compare the predicted maximum cluster mass with the observed values derived from the data in § 4.4. Because the masses were derived from PDFs rather than single best fit values, our estimated M_{max} is taken to be the point where the uncertainties on the mass distribution become more than 50% of the estimated value.

In Figure 13, The values for each brick are indicated by the black crosses, for which the spectral indices correspond to the best values obtained in §4.4.

The comparison between the predicted and observed values of M_{max} shows that the lack of massive clusters in B09 and B21 is consistent with the expectation for a stochastic sampling of a power-law mass distribution. In other words, there is no need to invoke mass truncation to explain the observed upper mass limits of the present day cluster mass function. The mass cut we observe in B15 ($M_{max} = 1.7 \times 10^5$ $M_\odot$) appears to be a factor of 2 smaller than the theoretical sampling prediction of the maximum mass ($M_{max} = 5.2 \times 10^5$ $M_\odot$). There are only $3 - 4$ clusters between the adopted M_{max} and the theoretical prediction value, which leads to large uncertainties at this regime. We therefore have adopted our more conservative value of M_{max}.

6. CONCLUSIONS

We have derived ages, masses and exintction for the Year 1 PHAT cluster sample (Johnson et al. 2012), by comparing the cluster integrated 6-filter fluxes with an extended version of the stochastically sampled model clusters presented in Fouesneau & Lançon (2010). The

locus of the collection of stochastic models in color space (e.g., Figure 2) shows excellent agreement with that of the collection of cluster observations. Clusters with broadband colors either bluer or redder than those of the traditional continuous models find a natural match with the models we used in this paper.

We generated the full joint probability distribution function of the age, mass, and extinction for each of the 601 individual clusters in the sample. We then combined their individual distributions into global cluster age and mass distributions, noting limits at which completeness issues in the sample become severe.

The sample of clusters spans the entire length of the age sequence and includes a significant number of clusters with masses well below 10^3 $M_\odot$. Only a few datasets have the ability to sample objects across a variety of stages in cluster evolution over such a large, uninterrupted mass range.

We find that the cluster age distribution shows a constant number of clusters over the last ~ 100 Myr, with a power-law decline at older ages (see Figs 7 & 11). At least above the mass of $10^{3.2}$ $M_\odot$, these results are consistent with M31 producing a constant number of clusters from 100 Myr ago to present, with little significant cluster disruption over this timescale.

The mass distribution derived from the analysis closely resembles the power-law distributions obtained from many other galaxies. Specifically, the overall power-law index of the mass distribution is consistent with the canonical value of -2. However, the current cluster sample suggests a possible radial variation of this distribution across the disk, with the shallowest power-law found in the region with the highest star formation rate.

When we study the entire PHAT survey, including lower masses and a larger sample of fainter clusters, the improved accuracy and time resolution achievable with the new stochastic methods will allow us to address new questions. Future work will account for the challenging determination of completeness and selection effects. In particular, the expected number of clusters in PHAT will eventually provide 5 times more clusters over a broad range of local environments, which will open the possibility to study local variations among cluster populations beyond our current the initial assessment in this study.

The authors acknowledge the efforts of the entire PHAT collaboration in this project. Also, the authors thank the Nate Bastian from is prompt and useful referee report. DG kindly acknowledges financial support by the German Research Foundation (DFG) through grant GO 1659/3-1. Support for DRW is provided by NASA through Hubble Fellowship grants HST-HF-51331.01 awarded by the Space Telescope Science Institute. This paper is based on observations taken with the NASA/ESA Hubble Space Telescope. Support for this work was provided by NASA through grant number HST GO-12055 from the Space Telescope Science Institute, which is operated by AURA, Inc., under NASA contract NAS5-26555.

REFERENCES

Barbaro, C., & Bertelli, C. 1977, A&A, 54, 243
Bastian, N., & Gieles, M. 2008, in Astronomical Society of the Pacific Conference Series, Vol. 388, Mass Loss from Stars and the Evolution of Stellar Clusters, ed. A. de Koter, L. J. Smith, & L. B. F. M. Waters, 353–+
Bastian, N., et al. 2011, MNRAS, 417, L6
—. 2012, MNRAS, 419, 2606
Baumgardt, H., & Makino, J. 2003, MNRAS, 340, 227
Bertelli, G., Bressan, A., Chiosi, C., Fagotto, F., & Nasi, E. 1994, A&AS, 106, 275
Bik, A., Lamers, H. J. G. L. M., Bastian, N., Panagia, N., & Romaniello, M. 2003, A&A, 397, 473
Billett, O. H., Hunter, D. A., & Elmegreen, B. G. 2002, AJ, 123, 1454
Bohlin, R. C. 2007, in Astronomical Society of the Pacific Conference Series, Vol. 364, The Future of Photometric, Spectrophotometric and Polarimetric Standardization, ed. C. Sterken, 315
Borissova, J., et al. 2011, A&A, 532, A131
Boutloukos, S. G., & Lamers, H. J. G. L. M. 2003, MNRAS, 338, 717
Bressan, A., Fagotto, F., Bertelli, G., & Chiosi, C. 1993, A&AS, 100, 647
Bruzual, G., & Charlot, S. 2003, MNRAS, 344, 1000
Caldwell, N., Schiavon, R., Morrison, H., Rose, J. A., & Harding, P. 2011, AJ, 141, 61
Cardelli, J. A., Clayton, G. C., & Mathis, J. S. 1989, ApJ, 345, 245
Cerviño, M., & Luridiana, V. 2004, A&A, 413, 145
Cezario, E., Coelho, P. R. T., Alves-Brito, A., Forbes, D. A., & Brodie, J. P. 2012, ArXiv e-prints
Chandar, R., Fall, S. M., & Whitmore, B. C. 2010, ApJ, 711, 1263
Chiosi, E., Vallenari, A., Held, E. V., Rizzi, L., & Moretti, A. 2006, A&A, 452, 179
Converse, J. M., & Stahler, S. W. 2011, MNRAS, 410, 2787
Dalcanton, J. J., et al. 2012, ArXiv e-prints
de Grijs, R., & Anders, P. 2006, MNRAS, 366, 295
Dolphin, A. E. 2002, MNRAS, 332, 91
Dowell, J. D., Buckalew, B. A., & Tan, J. C. 2008, AJ, 135, 823
Efron, B. 1987, Journal of the American Statistical Association, 82, pp. 171
Elmegreen, B. G., & Efremov, Y. N. 1997, ApJ, 480, 235
Elmegreen, B. G., & Hunter, D. A. 2010, ApJ, 712, 604
Fall, S. M., Chandar, R., & Whitmore, B. C. 2005, ApJ, 631, L133
—. 2009, ApJ, 704, 453
Fioc, M., & Rocca-Volmerange, B. 1997, A&A, 326, 950
Fouesneau, M., & Lançon, A. 2010, A&A, 521, A22
Fouesneau, M., Lançon, A., Chandar, R., & Whitmore, B. C. 2012, ApJ, 750, 60
Gieles, M., & Bastian, N. 2008, A&A, 482, 165
Gieles, M., & Portegies Zwart, S. F. 2011, MNRAS, 410, L6
Girardi, L., Chiosi, C., Bertelli, G., & Bressan, A. 1995, A&A, 298, 87
Groenewegen, M. A. T., & de Jong, T. 1993, A&A, 267, 410
Hodge, P. 1987, PASP, 99, 724
Hunter, D. A., Elmegreen, B. G., Dupuy, T. J., & Mortonson, M. 2003, AJ, 126, 1836
Johnson, L. C., et al. 2012, ArXiv e-prints
Kim, H., et al. 2012, ApJ, 753, 26
King, I. 1962, AJ, 67, 471
Kroupa, P., & Boily, C. M. 2002, MNRAS, 336, 1188
Kroupa, P., Tout, C. A., & Gilmore, G. 1993, MNRAS, 262, 545
Kroupa, P., Weidner, C., Pflamm-Altenburg, J., Thies, I., Dabringhausen, J., Marks, M., & Maschberger, T. 2013, The Stellar and Sub-Stellar Initial Mass Function of Simple and Composite Populations, ed. T. D. Oswalt & G. Gilmore, 115
Kumai, Y., Basu, B., & Fujimoto, M. 1993, ApJ, 404, 144
Lamers, H. J. G. L. M., Gieles, M., & Portegies Zwart, S. F. 2005, A&A, 429, 173
Larsen, S. S. 2009, A&A, 494, 539
Larsen, S. S., & Richtler, T. 2000, A&A, 354, 836
Lejeune, T., Cuisinier, F., & Buser, R. 1997, A&AS, 125, 229
Maíz Apellániz, J. 2009, ApJ, 699, 1938
McConnachie, A. W., Irwin, M. J., Ferguson, A. M. N., Ibata, R. A., Lewis, G. F., & Tanvir, N. 2005, MNRAS, 356, 979
McCrady, N., & Graham, J. R. 2007, ApJ, 663, 844
Parmentier, G., & de Grijs, R. 2008, MNRAS, 383, 1103
Piskunov, A. E., Kharchenko, N. V., Schilbach, E., Röser, S., Scholz, R., & Zinnecker, H. 2009, A&A, 507, L5
Popescu, B., & Hanson, M. M. 2010, in IAU Symposium, Vol. 266, IAU Symposium, ed. R. de Grijs & J. R. D. Lépine, 511–515
Popescu, B., Hanson, M. M., & Elmegreen, B. G. 2012, ApJ, 751, 122
Portegies Zwart, S. F., McMillan, S. L. W., & Gieles, M. 2010, ARA&A, 48, 431
Rafelski, M., & Zaritsky, D. 2005, AJ, 129, 2701

Rubin, D. B. 1981, The Annals of Statistics, 9, pp. 130
Searle, L., Wilkinson, A., & Bagnuolo, W. G. 1980, ApJ, 239, 803
Silva-Villa, E., Adamo, A., Bastian, N., Fouesneau, M., & Zackrisson, E. 2014, MNRAS letters, in press
Vansevičius, V., Kodaira, K., Narbutis, D., Stonkutė, R., Bridžius, A., Deveikis, V., & Semionov, D. 2009, ApJ, 703, 1872
Whitmore, B. C., Chandar, R., & Fall, S. M. 2007, AJ, 133, 1067
Whitmore, B. C., & Zhang, Q. 2002, AJ, 124, 1418
Whitmore, B. C., et al. 2011, ApJ, 729, 78
Zepf, S. E., & Ashman, K. M. 1993, MNRAS, 264, 611
Zhang, Q., & Fall, S. M. 1999, ApJ, 527, L81
Zurita, A., & Bresolin, F. 2012, ArXiv e-prints

APPENDIX

CATALOG

This Section present the catalog resulting from this study. Only a few entries are shown as an example describing the full content available online.

Here we present the catalog of parameter estimates derived in this study for the Johnson et al. (2012) star cluster catalog. A subset of the catalog is presented in the print version of the paper, with the full catalog being online.

In this table are given the cluster PHAT ID numbers and the coordinates of the clusters from Johnson et al. (2012). The "best" values are the coordinates of the (A_V - age - mass) triplet that maximizes the posterior distribution of the individual clusters. The other values are the ith-percentiles of the marginalized distributions over the two other parameters. The 16th and 84th percentiles are the equivalent limits of a 1-σ range for a Gaussian distribution (2.5th and 97.5th percentiles are the limits of a 2-σ confidence interval.)

TABLE 2
AGE-MASS AND EXTINCTION RESULTS FROM THE ANALYSIS WITH DISCRETE CLUSTER MODELS.

			A_V					$\log(A/yr)$					$\log(M/M_\odot)$					
PCNUM	RA[1]	DEC[1]	best[2]	p16[3]	p84	p2.5	p97.5	best	p16	p84	p2.5	p97.5	best	p16	p84	p2.5	p97.5	cflag [4]
1	11.63827	42.19389	0.9	0.6	1.2	0.6	1.2	6.75	6.53	6.96	6.32	6.96	3.18	2.35	3.45	2.35	3.73	0
2	11.63714	42.20994	0.3	0	0.6	0	0.6	6.53	6.32	6.75	6.32	7.18	3.18	2.90	3.45	2.90	3.73	0
29	11.62827	42.22423	0	0	0.3	0	0.3	8.47	8.25	8.68	8.25	8.68	3.45	3.18	3.73	3.18	3.73	0
34	11.59456	42.19844	0.3	0	1.5	0	2.4	8.68	8.04	9.11	7.39	9.33	2.35	1.80	2.90	1.53	3.18	0
35	11.62181	42.20984	0.9	0.6	1.2	0.6	1.2	6.96	6.53	7.18	6.53	7.18	2.08	1.80	2.63	1.53	2.63	0
...	...	...	...	...	...	...	...	*Full table available as electronic supplement*						...	...	...	...	
1725	11.58850	42.25820	1.2	0.3	2.1	0	2.4	7.61	6.75	8.25	6.10	8.47	2.63	2.08	3.18	1.53	3.18	0
1726	11.60538	42.26594	1.8	0.9	2.1	0	3	8.90	8.68	9.33	7.18	10.1	4.01	3.45	4.28	3.18	4.56	1
1728	11.58719	42.25828	0	0	1.5	0	2.4	8.04	6.10	8.25	6.10	8.68	2.08	1.53	2.90	1.53	3.18	0

[1] Significantly more figures are available in the electronic table
[2] "best" represents the triplet which maximize the posterior
[3] "pXX" represents the XX-th percentile of the marginalized posterior
[4] flag suspicious fit from visual CMD inspection (boolean value)